

FLUX CALIBRATED EMISSION LINE IMAGING OF EXTENDED SOURCES USING GTC/OSIRIS TUNABLE FILTERS*

Y. D. MAYYA^{1,6}, D. ROSA GONZÁLEZ¹, O. VEGA¹, J. MÉNDEZ-ABREU^{2,3}, R. TERLEVICH^{1,4}, E. TERLEVICH^{1,5}, E. BERTONE¹,
 L. H. RODRÍGUEZ-MERINO¹, C. MUÑOZ-TUÑÓN^{2,3}, J. M. RODRÍGUEZ-ESPINOSA^{2,3}, J. SÁNCHEZ ALMEIDA^{2,3}, J. A. L. AGUERRI^{2,3}

Draft version February 25, 2013

ABSTRACT

We investigate the utility of the Tunable Filters (TFs) for obtaining flux calibrated emission line maps of extended objects such as galactic nebulae and nearby galaxies, using the Optical System for Imaging and low Resolution Integrated Spectroscopy (OSIRIS) at the 10.4-m *Gran Telescopio Canarias* (GTC). Despite the relatively large field of view of OSIRIS ($8' \times 8'$), the change in wavelength across the field ($\sim 80 \text{ \AA}$) and the long-tail of the TF spectral response function are hindrances for obtaining accurate flux calibrated emission-line maps of extended sources. The purpose of this article is to demonstrate that emission-line maps useful for diagnostics of nebula can be generated over the entire field of view of OSIRIS, if we make use of theoretically well-understood characteristics of TFs. We have successfully generated the flux-calibrated images of the nearby, large late-type spiral galaxy M101 in the emission lines of H α , [N II] $\lambda 6583$, [S II] $\lambda 6716$ and [S II] $\lambda 6731$. We find that the present uncertainty in setting the central wavelength of TFs ($\sim 1 \text{ \AA}$), is the biggest source of error in the emission-line fluxes. By comparing the H α fluxes of HII regions in our images with the fluxes derived from H α images obtained using narrow-band filters, we estimate an error of $\sim 11\%$ in our fluxes. The flux calibration of the images was carried out by fitting the Sloan Digital Sky Survey (SDSS) *griz* magnitudes of in-frame stars with the stellar spectra from the SDSS spectral database. This method resulted in an accuracy of 3% in flux calibration of any narrow-band image, which is as good as, if not better than, that feasible using the observations of spectrophotometric standard stars. Thus time-consuming calibration images need not be taken. A user-friendly script under the IRAF environment was developed and is available on request.

Subject headings: galaxies: photometry — ISM: HII regions — methods: data analysis — techniques: image processing

1. INTRODUCTION

Optical System for Imaging and low Resolution Integrated Spectroscopy (OSIRIS) is an imager and spectrograph for the optical wavelength range, located in the Nasmyth-B focus of the 10.4-m *Gran Telescopio Canarias* (GTC) (Cepa et al. 2005; Cepa 2010). Apart from the standard broad-band imaging and long-slit spectroscopy, it provides additional capability such as narrow-band tunable filter (TF) imaging, charge-shuffling and multi-object spectroscopy. OSIRIS covers the wavelength range from 0.365 to $1.05 \mu\text{m}$ with an unvignetted field of view (FoV) of $7.8 \times 7.8 \text{ arcmin}^2$, for direct imaging. Narrow-band imaging is made possible through the use of a TF, which is in essence a low resolution Fabry-Perot etalon. The filter is tuned by setting

a specific separation between the optical plates of the Fabry-Perot. OSIRIS has two different TFs: one for the blue range ($3750\text{--}6750 \text{ \AA}$; yet to be commissioned), and another for the red range ($6510\text{--}9350 \text{ \AA}$). In this work, we describe the results for the latter (red) etalon.

The relatively large FoV on a 10-m telescope, combined with the tunable nature of the filters, opens up a new method of observation, which can be useful in a variety of astrophysical contexts, both galactic and extragalactic. The use of narrow-band filters, adequately defined to map certain spectral regions, allows the detailed study at seeing-limited resolution, of the spatial distribution of the ionized gas properties and recent star formation, and of the associated stellar populations. Flux calibrated images in the bright lines of hydrogen, oxygen, nitrogen and sulphur in the optical, allow us to map, among other parameters, the metallicity gradients in galaxies using imaging techniques rather than the time-consuming spectroscopic techniques that are in use currently (Rosales-Ortega et al. 2010). This has motivated recently built large telescopes such as the 11-m South African Large Telescope (Rangwala et al. 2008) or the Magellan Baade 6.5-m telescope (Veilleux et al. 2010) to have TFs for imaging. We are presently engaged in a survey of galaxies in the local universe (LUS⁷= Local Universe Survey) that includes all galaxies inside a volume of 3.5 Mpc in radius that are visible from La Palma.

*BASED ON OBSERVATIONS MADE WITH THE GRAN TELESCOPIO CANARIAS (GTC), INSTALLED IN THE SPANISH OBSERVATORIO DEL ROQUE DE LOS MUCHACHOS OF THE INSTITUTO DE ASTROFÍSICA DE CANARIAS, IN THE ISLAND OF LA PALMA.

¹ Instituto Nacional de Astrofísica, Óptica y Electrónica, Tonantzintla, Puebla, C.P. 72840, Mexico.

² Instituto de Astrofísica de Canarias, E-38205 La Laguna, Tenerife, Spain.

³ Departamento de Astrofísica, Universidad de La Laguna, Tenerife, Spain.

⁴ IoA, Madingley Rd., Cambridge CB3 0HA, UK.

⁵ Visiting Fellow, IoA, Madingley Rd., Cambridge CB3 0HA, UK.

⁶ ydm@inaoep.mx

⁷ <http://www.inaoep.mx/~gtc-lus/>

IFU observations of these galaxies present two problems: IFU observations would represent a huge drop in spatial resolution and, with a median D_{25} of $4.5'$, they are too large to be observed even with the largest available IFU.

Lara-López et al. (2010) used template spectra typical of star-forming galaxies to estimate the errors in derived flux for extragalactic point-like sources on the OSIRIS TF images. However, photometric accuracy of the TF images of extended objects using observed data is yet to be evaluated. In this study, we explore the capabilities of TF for obtaining flux calibrated images using observations acquired with OSIRIS TF. The OSIRIS etalon is placed in a converging beam, which results in the variation of the effective wavelength over the FoV (Born & Wolf 1980). For the red etalon, the change is as much as 80 \AA over the $4'$ radius, thus limiting the monochromatic FoV to less than $2'$ radius (Méndez-Abreu et al. 2011). In addition, the TF spectral response function (see Eq. 2) has a long tail, which difficults the flux calibration of a faint line in the neighborhood of a bright one. For example $H\alpha$ line contaminates even if the TF is tuned to detect the $[N II]\lambda 6583$ line. Given that these characteristics of TF are well-understood, flux calibrated monochromatic images over the entire FoV can be obtained using a tailor-made post-observation reconstruction software.

The fact that the filters are tunable, in addition, creates its own problems for absolute flux calibration due to the non-standard nature of the filters. Observing spectrophotometric standard stars at each tuned wavelength is a solution, but it is costly in terms of telescope time. Alternatively, small telescopes could be used to carry out spectrophotometric observations of the in-frame field stars. The recent Sloan Digital Sky Survey (SDSS) spectrophotometric survey of field stars (Beers et al. 2006; Abazajian et al. 2009) offers an attractive solution to the problem, that does not require any telescope time for calibration purposes. In this paper, we explore the use of this database to spectrophotometrically calibrate the in-frame SDSS photometric stars.

In §2, we describe the data used in this work. The method we followed for reconstructing a monochromatic image and its implementation are described in §§3 and 4, respectively. The sensitivity of the reconstructed emission line fluxes to various observational parameters is studied using simulated images in §5 where we also suggest guidelines for planning imaging observations with OSIRIS/TF. The flux calibration technique and accuracy are described in §6. $H\alpha$ fluxes of selected $H II$ regions in the reconstructed image are compared to an $H\alpha$ image obtained in a traditional way in §7. The results of this study are summarized in §8.

2. DESCRIPTION OF THE DATA FOR RECONSTRUCTION

2.1. The OSIRIS detector and image formats

OSIRIS uses two CCDs of 2048×4102 pixel format to cover its total FoV of $8' \times 8'$, with a physical gap of $\sim 9''$ between the two CCDs. Each one has 50 additional overscan pixels at the beginning of the array, thus resulting in a format of 2098×4102 for each image. The optical center of OSIRIS lies in the central gap as described in Méndez-Abreu et al. (2011) and also in

TABLE 1
GTC OBSERVING BLOCKS SUMMARY

Observing Block	λ_c (\AA)	FWHM (\AA)	Order Sorter Filters	Exp. Time (seconds)
$H\alpha+[N II]$	6528	18	f648/28	2×180
	6548	18	f648/28	2×180
	6568	18	f648/28	2×180
	6588	18	f657/35	2×180
	6608	18	f657/35	2×180
	6628	18	f657/35	2×180
	6648	18	f657/35	2×180
	6668	18	f657/35	2×180
	6688	18	f666/36	2×180
	6696	18	f666/36	3×180
[S II]	6716	18	f666/36	3×180
	6736	18	f666/36	3×180
	6756	18	f666/36	3×180
	6776	18	f680/43	3×180
	6796	18	f680/43	3×180
	6816	18	f680/43	3×180

the OSIRIS User Manual⁸. Astrometric calibration is required before being able to mosaic the images registered in the two CCDs. By performing astrometry of 10 stars on each CCD that are distributed over the entire FoV, we found that the image scale is slightly different for the two CCDs. The left and right CCDs have values of $0.127''/\text{pixel}$ and $0.129''/\text{pixel}$, respectively, with an average value of $0.128''/\text{pixel}$. This average value agrees well with the theoretically expected value of the plate scale for the GTC/OSIRIS instrument parameters listed in Table 1 of Méndez-Abreu et al. (2011).

2.2. OSIRIS TF emission-line imaging of M101

We illustrate the reconstruction technique using observations of M101 aimed at obtaining continuum-free images of the $H\alpha$, $[N II]\lambda 6583$, $[S II]\lambda 6716$ and $[S II]\lambda 6731$ emission lines over a FoV of $8' \times 8'$. The observations were carried out at the GTC in two observing runs on June 22 and 26 in 2009, the former for the $[S II]\lambda 6716, 6731$ lines and the latter for the $H\alpha$, $[N II]\lambda 6583$ lines. Table 1 describes the details of these two observing runs. The telescope pointing remained the same for all images (wavelengths) constituting a TF scan. The telescope position was then dithered by $6''$ and the entire sequence was repeated. This was done in order to facilitate removal of any detector artefacts. For a given region in the galaxy, the two dithered TF images have slightly different wavelength and hence different response for the detection of a line. Thus it is important to take into account these response differences before coadding them. We handled the dithered image sets as independent sets of data and used them to estimate internal errors in the flux calibration (see §6). For the $H\alpha+[N II]$ scan, observations were carried out at two dithered positions (P1 and P2, henceforth), whereas for the $[S II]$ scan, three dithered positions were used (P1, P2 and P3, henceforth).

Initial reduction of the images for correcting for BIAS was done independently for the two CCDs constituting an image. Reliable flat-field frames were not available

⁸ http://www.gtc.iac.es/en/media/documentos/OSIRIS-USER-MANUAL_v1.1.pdf

for the set of data we were analyzing, hence no attempts were made to correct for this. Typical pixel-to-pixel errors in response are expected to be less than 1% for the CCD chips used. Stars in the field of each of the two CCDs were independently analyzed to obtain the astrometric solution between the pixel and equatorial coordinates, using the SDSS coordinates of around 10 stars in the observed field as reference. The two CCDs were then stitched together to form a single image, free of all geometrical distortions. The procedure is repeated for the other scans.

3. MONOCHROMATIC IMAGE RECONSTRUCTION TECHNIQUE

3.1. Basic formulae for tunable filters

The effective wavelength λ_r at a distance r from the optical center of the tunable filter (TF) changes following the law (Méndez-Abreu et al. 2011; Beckers 1998):

$$\lambda_r = \frac{\lambda_c}{\sqrt{1 + 6.5247 \times 10^{-9} r^2}}, \quad (1)$$

where λ_c is the wavelength at the optical center. The coefficient of r^2 is the inverse square of the effective focal length of the camera, with r expressed in physical units of pixels of $15\mu\text{m}$ in size. Due to the geometrical distortions of the images, a given λ_r moves to a different radial distance r' in the astrometrically calibrated images. We used the astrometric solution to map the new wavelengths $\lambda_{r'}$ at each astrometrically calibrated image with resampled pixels of $0.125''$ in size. This correction, which is not symmetric around the optical center, increases quadratically with radial distance from the optical center, reaching values of ~ 2 and ~ 5 Å at $4'$ away from the optical center on the left and right CCDs, respectively.

For a TF of Full Width at Half Maximum FWHM, the filter response for a certain wavelength λ (e.g. the H α line) in a pixel where the nominal wavelength is λ_r , is given by:

$$R_\lambda(r) = \left(1 + \left[\frac{2(\lambda - \lambda_r)}{FWHM} \right]^2 \right)^{-1}. \quad (2)$$

This equation is an approximation valid when the free spectral range (i.e. the wavelength separation between adjacent orders) is much larger than the spectral purity (i.e. the smallest measurable wavelength difference) — see, e.g., Jones et al. (2002). The ratio between free spectral range and spectral purity is called finesse and is a critical parameter of all TFs. In the case of OSIRIS, the finesse is of the order of 50 (see OSIRIS User Manual), which allows the use of Eq. 2 (Jones et al. 2002). Spectral purity and FWHM coincide when the finesse is large. The wavelength at the optical center (λ_c in Eq. 1) as well as the FWHM are set by tuning the etalon. In our observations the FWHM was set to 18 Å (see Table 1) rendering a free spectral range of the order of 900 Å.

A monochromatic image at a particular wavelength (e.g. H α) over the entire FoV of the detector can be obtained if we have a sequence of images where λ_c between successive images increases by $\lesssim FWHM$. For the image sequences we have, this criterion was not strictly met ($\Delta\lambda$ between successive images was 20 Å for a $FWHM=18$ Å). The consequence of this is that there are annular zones

with missing data. However, multiple observations with dithered positions helped us to fill-in data for these zones. In what follows we describe the method we have adopted for reconstructing a monochromatic image from M101 image sequences.

3.2. Reconstruction Strategy

The observed count rate $F(x, y)$ at a pixel x, y of an image is related to the emitted intensity $I_\lambda(x, y)$ by the equation:

$$F(x, y) = \frac{\int I_\lambda(x, y) R_\lambda(r) d\lambda}{\kappa} + \text{Sky}(x, y) \quad (3)$$

where $R_\lambda(r)$ (Eq. 2) is the value of the response curve at a distance $r = \sqrt{(x - x_0)^2 + (y - y_0)^2}$ from the optical center (x_0, y_0) , κ is the conversion factor between the intensity and the count rate in units of $\text{erg cm}^{-2} \text{s}^{-1} / (\text{count s}^{-1})$, and $\text{Sky}(x, y)$ is the count rate from the sky at a pixel x, y . In §6, we describe a procedure to determine the value of κ . Ideally, the sky term can be estimated if observations of sky frames are taken in each scanned wavelength. Given that this involves extra telescope time, such observations were not carried out. The dependence of sky on x, y is because of two causes (1) an intrinsic spatial variation of the sky, and (2) a wavelength dependence of sky emission. The first of these can be assumed to be negligible over the FoV of OSIRIS and hence the sky variation in the image is principally due to the second effect. Given the circular symmetry of the variation of wavelength, sky values are radially symmetric around the optical center, i.e. $\text{Sky}(x, y) \equiv \text{Sky}(r)$. We determined $\text{Sky}(r)$ as the average count rate from the sky pixels in annular zones of $\text{width}=FWHM/2$.

In general, I_λ includes two contributions: (1) I_{line} , emission line flux integrated over the line profile, and (2) I_{cont} , the continuum flux density. We first describe the method for reconstructing monochromatic images in the simplest case of only one emission line entering the filters in the entire scanned wavelength range. The emission lines from nebular sources are extremely narrow with respect to the typical bandwidth of the TF, and hence the count rate from a line depends only on the value of the response function at the wavelength of the line, $R_{\text{line}}(r)$. Hence the integral can be replaced by a simple multiplication, i.e. $\int I_{\text{line}}(x, y) R_\lambda(r) d\lambda = I_{\text{line}}(x, y) R_{\text{line}}(r)$, when line-width $\ll FWHM$. On the other hand, the term due to the continuum from the source is $\frac{\int I_{\text{cont}}(x, y) R_\lambda(r) d\lambda}{\kappa} \equiv \text{Cont}(x, y)$, where $\text{Cont}(x, y)$ is the observed count rate in the continuum image. With these approximations Eq. 3 can be re-written as:

$$F(x, y) = \frac{I_{\text{line}}(x, y) R_{\text{line}}(r)}{\kappa} + \text{Cont}(x, y) + \text{Sky}(r). \quad (4)$$

A trivial manipulation of the above equation gives:

$$I_{\text{line}}(x, y) = \frac{\kappa (F(x, y) - \text{Cont}(x, y) - \text{Sky}(r))}{R_{\text{line}}(r)} \quad (5)$$

By making a simple substitution

$$C(x, y) = F(x, y) - \text{Cont}(x, y) - \text{Sky}(r), \quad (6)$$

where $C(x, y)$ is the sky and continuum subtracted count rate at a position x, y of the image, the above equation can be re-written as:

$$I_{\text{line}}(x, y) = \frac{\kappa C(x, y)}{R_{\text{line}}(r)}. \quad (7)$$

Due to the long tail of the response curves, an emission line from some regions of the galaxy is registered by more than one image of the scan. Hence, in general, simultaneous equations of the kind of Eq. 7 can be written for each image. The line contribution in the two adjacent images can be combined, with the weights for combining being determined by the values of the response functions for the line at each pixel. A generalized equation for recovering the flux from any pixel where the line is registered by two consecutive images of a scan: $im1$ and $im2$, can be written as:

$$I_{\text{line}}(x, y) = \frac{[\kappa C(x, y)]_{im1} + [\kappa C(x, y)]_{im2}}{[R_{\text{line}}(r)]_{im1} + [R_{\text{line}}(r)]_{im2}} \quad (8)$$

For the sake of compactness, from now onwards $R_{\lambda}(r)$ will be denoted simply by R_{λ} .

3.3. $H\alpha$ and $[S II]$ scans

Due to the long tail of the TF response curve, an emission line separated from the target line by $\sim FWHM$ contributes non-negligibly to the flux received in the image. This is the case while mapping the $H\alpha$ line with a tunable filter of $FWHM \sim 18 \text{ \AA}$, where the contribution of the flanking $[N II]$ lines to the observed flux cannot be neglected. The contribution from an unwanted line becomes even more important while trying to recover the $[N II]$ lines, as the $H\alpha$ line is likely to dominate the observed flux, rather than the $[N II]$ lines. Another interesting case is that of the $[S II]$ doublet, where both lines contribute in most of the images of a typical TF scan. These cases can be easily treated by adding more terms — one term such as $I_{\text{line}}(x, y)R_{\text{line}}(r)$ for each emission line — to the numerator of the first term in Eq. 4. For the scan involving the $H\alpha$ line, the first term in the *numerator* of Eq. 4 should be replaced by:

$$I_{\text{line}}(x, y)R_{\text{line}} \rightarrow I_{H\alpha}R_{\lambda H\alpha} + I_{6583}R_{\lambda 6583} + I_{6548}R_{\lambda 6548}, \quad (9)$$

where $R_{\lambda H\alpha}$, $R_{\lambda 6583}$, and $R_{\lambda 6548}$ are the values of the response function at a radial distance r from the optical center for the observed (not the rest-frame) wavelengths of the corresponding lines.

Eq. 7 for the $H\alpha$ line can then be re-written as,

$$I_{H\alpha}(x, y) = \frac{\kappa C(x, y)}{R_{\lambda H\alpha} + \frac{I_{6548}}{I_{6583}}(R_{\lambda 6583} + \frac{1}{3}R_{\lambda 6548})}, \quad (10)$$

where we have substituted the value of the intrinsic flux ratio of $\frac{I_{6548}}{I_{6583}} = \frac{1}{3}$. The equation has a term involving $\frac{I_{6583}}{I_{H\alpha}}$ in the denominator. Thus in order to reconstruct the $H\alpha$ line image, we need to know *a priori* the flux ratio images of the contaminating $[N II]\lambda 6583$ line with respect to the $H\alpha$ line. The $[N II]$ line fluxes, on the other hand, require a knowledge of the $H\alpha$ flux, as can be seen

by the equation for the $[N II]\lambda 6583$ line:

$$I_{6583}(x, y) = \frac{\kappa C(x, y) - I_{H\alpha}(x, y)R_{\lambda H\alpha}}{R_{\lambda 6583}}. \quad (11)$$

In this equation, we have neglected the $[N II]\lambda 6548$ line contribution given that it contributes less than 2% in image sections tuned to maximize the $[N II]\lambda 6583$ emission. Thus, in order to obtain $[N II]\lambda 6583$ flux map, we need to know the $H\alpha$ flux. An iterative procedure involving Eqs. 10 and 11 is necessary for an accurate recovery of both $H\alpha$ flux and $\frac{I_{6583}}{I_{H\alpha}}$ ratio. Given the exploratory nature of the present study, we have calculated the $H\alpha$ fluxes by fixing $\frac{I_{6583}}{I_{H\alpha}} = 0.1$ for all regions. This approximation would result in an overestimation of the $H\alpha$ fluxes by $> 2.5\%$, and underestimation of the $\frac{I_{6583}}{I_{H\alpha}}$ ratios by ~ 0.1 for regions having intrinsic $\frac{I_{6583}}{I_{H\alpha}} \gtrsim 0.2$.

The reconstruction equations for the $\lambda 6716$ and $\lambda 6731$ lines from the $[S II]$ scan are:

$$I_{6716}(x, y) = \frac{[\kappa C(x, y)]_{im1} + [\kappa C(x, y)]_{im2}}{R_{\lambda 6716}^{im1} + R_{\lambda 6716}^{im2} + \frac{I_{6731}(x, y)}{I_{6716}(x, y)}(R_{\lambda 6731}^{im1} + R_{\lambda 6731}^{im2})}, \quad (12)$$

and

$$I_{6731}(x, y) = \frac{[\kappa C(x, y)]_{im1} + [\kappa C(x, y)]_{im2}}{R_{\lambda 6731}^{im1} + R_{\lambda 6731}^{im2} + \frac{I_{6716}(x, y)}{I_{6731}(x, y)}(R_{\lambda 6716}^{im1} + R_{\lambda 6716}^{im2})}, \quad (13)$$

In these equations, $im1$ and $im2$ denote the image sections tuned to maximize the $\lambda 6716$ and $\lambda 6731$ lines, respectively. Note that, in order to recover the I_{6716} image, we need the I_{6731} image and vice versa. Unlike the case of $\frac{I_{N II}}{I_{H\alpha}}$, no apriori values for the intensity ratios of the $[S II]$ lines could be used, given that this ratio is very sensitive to the electron density of the regions. We hence resolved Eqs. 12 and 13 by assuming a value of $\frac{I_{6716}}{I_{6731}}$, and iteratively changing that value until the value at every pixel stabilizes within 10% in two successive iterations. We checked that the resulting images are the same irrespective of the starting value of $\frac{I_{6716}}{I_{6731}}$.

4. IMPLEMENTATION OF THE METHOD

We developed a script under the IRAF⁹ environment to implement the method in a user-friendly way. The first step of the reconstruction process is obtaining wavelength *vs.* pixel look-up images for every image of the scan. These images are created using Eq. 1 and the astrometric solutions as described in §3.1. Values of λ_c ¹⁰ and FWHM are taken from Table 1. For each of the emission lines, we then created 2-dimensional response images using Eq. 2. The procedure we followed is illustrated using

⁹ IRAF is distributed by the National Optical Astronomy Observatory, which is operated by the Association of Universities for Research in Astronomy (AURA) under cooperative agreement with the National Science Foundation.

¹⁰ Wavelength calibration lamps were not supplied in this initial observing run, and hence we checked/recalibrated the value of λ_c by comparing the filter-convolved SDSS spectra of 7 $H II$ regions to the profiles of the corresponding $H II$ regions formed using the observed fluxes in successive images. Error in λ_c using this method is found to be $\lesssim 2 \text{ \AA}$, which is better than what could be achieved using the sky rings.

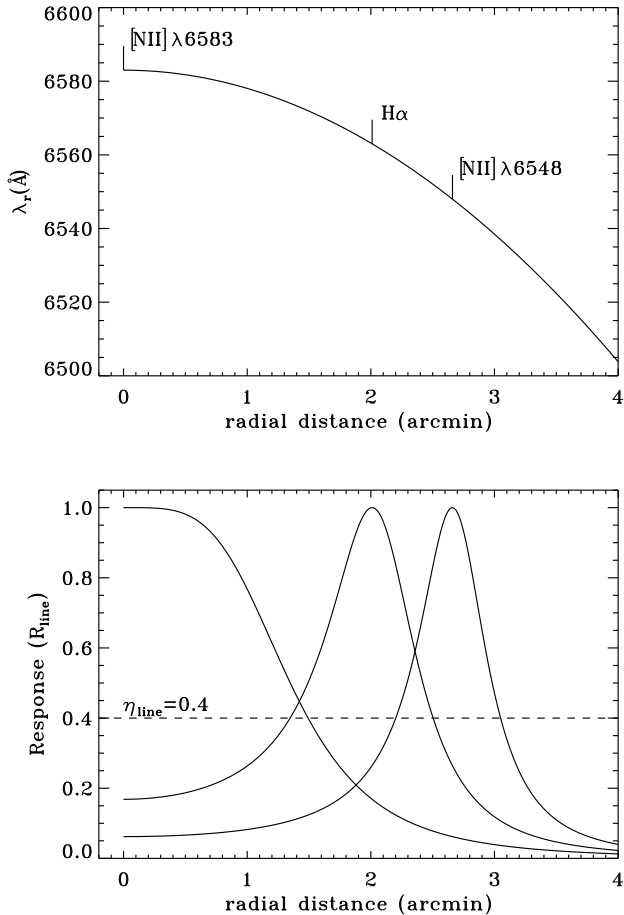


FIG. 1.— (Top) An illustration of the variation of the wavelength over the OSIRIS FoV as expected from Eq. 1, with $\lambda_c = 6588 \text{ \AA}$ (observed wavelength of $[\text{N II}]\lambda 6583$ line in M101) and $\text{FWHM} = 18 \text{ \AA}$. The positions where $[\text{N II}]\lambda 6583$, $\text{H}\alpha$, $[\text{N II}]\lambda 6548$, lines have maximum response are marked. (Bottom) The response curves, as calculated using Eq. 2, for each of these lines are shown. The part of the curves above the horizontal line ($\eta_{\text{line}} = 0.4$) can be used to reconstruct the monochromatic images in the corresponding lines.

1-d cuts on one of these images in Fig. 1. Specifically, we chose the image with $\lambda_c = 6588 \text{ \AA}$ for illustration, as this image is capable of detecting three different emission lines at different radial bins. The bottom panel shows the expected value of the response functions for the three lines as a function of the radial distance from the optical center. In cases such as this, where more than one emission line is registered within the $8' \times 8'$ FoV ($r = 4'$), a second line starts contributing significantly before the line of interest drops to below $\sim 50\%$ response, as illustrated in the bottom panel of Fig. 1. It is possible to isolate the contribution of each line by selecting only those zones where the line of interest has a response value above a certain level, as described below.

4.1. Choosing the value for the response cut-off

The part of a TF image that can be considered monochromatic is decided by the value for the response cut-off (η_{line}) parameter. By carefully choosing η_{line} ,

it is possible to reconstruct a monochromatic image in the line of interest even in the presence of contaminating lines. Only those pixels with a response value $R_{\text{line}} > \eta_{\text{line}}$ will be considered good for reconstructing the monochromatic image in that *line*. All these pixels belong to an annular zone of particular width (circle in the case of a line falling close to the optical center). For example, with $\eta_{\text{line}} = 0.4$, the image sections for reconstructing the $\text{H}\alpha$ and $[\text{N II}]\lambda 6583$ lines in the $\lambda_c = 6588 \text{ \AA}$ image correspond to the radial zones where the curve lies above the horizontal line in Fig. 1.

Two guidelines are useful for setting the value of η_{line} : (1) the response for the contaminating line in the selected image section has to be less than that for the main line, (2) there are no annular gaps in the final reconstructed image. The first condition depends on the wavelength difference between the contaminating lines, whereas the difference between central wavelengths of successive images of the scan ($\Delta\lambda_c$) determines the fulfillment of the second condition. For the case of $\text{H}\alpha$ and $[\text{N II}]\lambda 6583$, the response value would be the same at a wavelength mid-way between the two lines (i.e. 6573 \AA at rest-frame or 6578 \AA for our M101 scan given its recession velocity of 214 km s^{-1}). At radial zones where $\lambda_r < 6578 \text{ \AA}$, the observed count rates would be predominantly from the $\text{H}\alpha$ line, implying $\eta_{\text{line}} \geq 0.45$. On the other hand, the second criterion requires that λ_r be separated from $\lambda_{\text{H}\alpha}$ by at least $\Delta\lambda_c/2$, implying $\eta_{\text{line}} \leq 0.45$ for our M101 scan. Thus $\eta_{\text{line}} = 0.45$ is the optimal value for our dataset. The value of η_{line} could be marginally higher than this if dithered images are able to fill in data-less annular zones, or lower if the contaminating line contribution could be subtracted to within a few percent accuracy using an iterative procedure. For example, for our M101 scan, dithering between the images was sufficient to be able to fill-in the data gaps for $\eta_{\text{line}} = 0.5$. On the other hand, the SNR of the $[\text{N II}]\lambda 6583$ images was not good enough to iteratively subtract the $[\text{N II}]\lambda 6583$ contamination in the predominantly $\text{H}\alpha$ pixels. The user would be required to select the value of η_{line} based on the data parameters and the specific scientific objective.

4.2. Coadding monochromatic image sections

In Fig. 2, we show the response for the $\text{H}\alpha$ line in consecutive images of a TF scan. For a value of $\eta_{\text{line}} = 0.4$, in certain ranges of radial zones, the line is registered in two consecutive images. Thus, for $\eta_{\text{line}} = 0.4$ there is redundant data for some pixels for the construction of the monochromatic images. This redundancy can be used to our advantage to get deeper images, by coadding the pixel values from both images that contribute to that zone. The response curves are also coadded to get a net response curve such as shown by the solid line in Fig. 2. The coadded line image is divided by the net response image to get the entire image in the same flux scale (see Eq. 8).

4.3. Preparation of the continuum and sky images

Fundamental to the reconstruction process is the determination of pure count rate in the line $C(x, y)$ from the observed count rate $F(x, y)$. This is carried out through Eq. 6, which involves the estimation of sky and continuum images. The sky count rates $Sky(r)$ are calculated

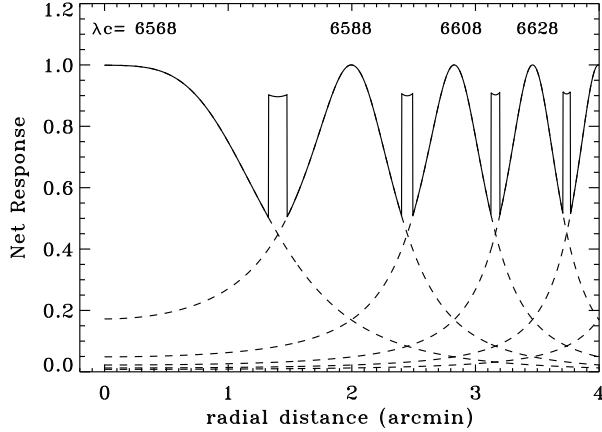


FIG. 2.— The net response curve for the reconstruction of the H α image for $\eta_{\text{line}} = 0.4$ is shown by the solid curve. H α response curves in individual TF images are shown by the dashed lines. The central wavelength λ_c (in Å) for each image is indicated above the corresponding response function.

as the median values in semi-annular zones, with a width equal to $FWHM/2 = 9$ Å.

The bluest wavelength of our scans is $\lambda_c = 6528$ Å, which is the filter with least contamination from any emission line. We used this image as a first-guess image of the continuum. Even for this filter, the H α line contributes more than 3% for pixels closer than $90''$ from the optical center. We defined a parameter η_{cont} such that only those pixels for which the response to detect any line does not exceed η_{cont} are considered for continuum (i.e. only pixels with $R_{\text{line}} < \eta_{\text{cont}}$). For example, for the image with $\lambda_c = 6528$ Å, with $\eta_{\text{cont}} = 0.03$ only pixels that are more distant than $90''$ from the optical center satisfy this condition. Even for these pixels, we estimated the line contribution using the reconstructed emission line maps, and subtracted it from the continuum pixels. Individual sections contributing to the continuum are stitched together (averaged when more than one image contributes to a pixel) to obtain the final continuum image. This image is input as the new continuum image and the entire process is repeated. From the simulated data (see §5.3, *Run 1*), we found that the continuum values converge after 3 iterations. A small value of η_{cont} would result in various annular zones where there are no pixels satisfying the condition $R_{\text{line}} < \eta_{\text{cont}}$. From simulated data, we found that line-free continuum images could be obtained even for η_{cont} as large as 0.2.

An IRAF package containing the scripts developed as part of this work is available to users upon request and will be available for downloading from the LUS webpage <http://www.inaoep.mx/~gtc-lus/>.

5. FLUX ERRORS IN THE RECONSTRUCTED IMAGES

5.1. Flux error due to tuning error

The central wavelength of the OSIRIS TF can be set only to an accuracy of 1 Å (See OSIRIS TF User Manual). This uncertainty in tuning the TF leads to an error in the recovered emission line fluxes. The error (δF) in flux (F) due to an uncertainty of $\delta\lambda_c$ in setting the cen-

tral wavelength depends directly on the first derivative of the response function (Eq. 2) with respect to λ .

$$\text{i.e.} \quad \frac{\delta F}{F} \equiv \frac{\delta R_\lambda}{R_\lambda} \equiv \frac{1}{R_\lambda} \left(\frac{\partial R_\lambda}{\partial \lambda} \right) \delta\lambda_c \quad (14)$$

Substituting the value of $\frac{\partial R_\lambda}{\partial \lambda}$, we get

$$\frac{\delta F}{F} = 4R_\lambda \left(\frac{\delta\lambda_c}{FWHM} \right) \sqrt{\left(\frac{1}{R_\lambda} - 1 \right)}. \quad (15)$$

Maximum error is introduced for image pixels where the TF response R_λ for the line of interest is 0.5. Thus, flux errors in the reconstructed image can be reduced if we use $\eta_{\text{line}} > 0.5$. It may be recalled from the analysis in §4.1 that the lower limit of η_{line} depends on $\Delta\lambda_c$. In order to have $\eta_{\text{line}} > 0.5$, $\Delta\lambda_c$ should be less than the $FWHM$.

We used the Eq. 15 to calculate the errors in the line fluxes, and summed the errors in quadrature to calculate the errors in the flux ratios, for nominal value of $\delta\lambda_c = 1$ Å. Our results are summarized in Fig. 3. In the three panels, we plot the errors in the calculated H α fluxes (top), the [N II] $\lambda 6583$ /H α ratio (middle) and [S II] $\lambda 6717/6731$ ratio (bottom) as a function of the sampling parameter, for two extreme values of FWHM permitted by the TF. The value of η_{line} is calculated in such a way that there are neither gaps nor overlapping pixels in the reconstructed image for a given sampling $\Delta\lambda_c$.

The most notable characteristic in these plots is that the errors in all these three quantities are lower for larger values of FWHM. This may seem counter-intuitive, and is the result of a sampling error of 1 Å being a larger fraction of $FWHM = 12$ Å than that for $FWHM = 18$ Å. In other words, the TF response function falls less steeply for larger FWHM, thus resulting in little errors as compared to that for smaller FWHMs. As expected, finer sampling results in smaller errors on the derived quantities, especially when the sampling rate is less than $0.7 \times FWHM$.

Line fluxes can be calculated with better accuracy than the flux ratios. The error in the [N II] $\lambda 6583$ /H α flux ratio takes into account the contamination by H α in the [N II] $\lambda 6583$ filters. This cross talk also makes the errors on the [N II] $\lambda 6583$ line flux marginally larger than those for the H α flux. The calculated errors on the individual [S II] line fluxes are similar to that for the H α flux.

It may be noted that a recessional velocity of 45 km s^{-1} produces a shift of 1 Å in the wavelength. Thus, in regions where kinematic deviations of this order or more are likely to exist (e.g. nuclear regions of galaxies), kinematical data are required for an accurate flux calibration. In the absence of such data, eq. 15 can be used, where $\delta\lambda_c$ is to be replaced by the uncertainty in the wavelength due to Doppler effect, to estimate the flux errors due to kinematic deviations.

5.2. Reconstruction of simulated TF images

The dataset we have for M101 is reconstructed with $\eta_{\text{line}} = 0.5$, implying maximum errors of around 11% in the recovered H α fluxes according to Fig. 3. In order to check the implementation of the equations of §3 in our reconstruction scripts, we need datasets with much smaller errors. We hence created artificial datasets by simulating

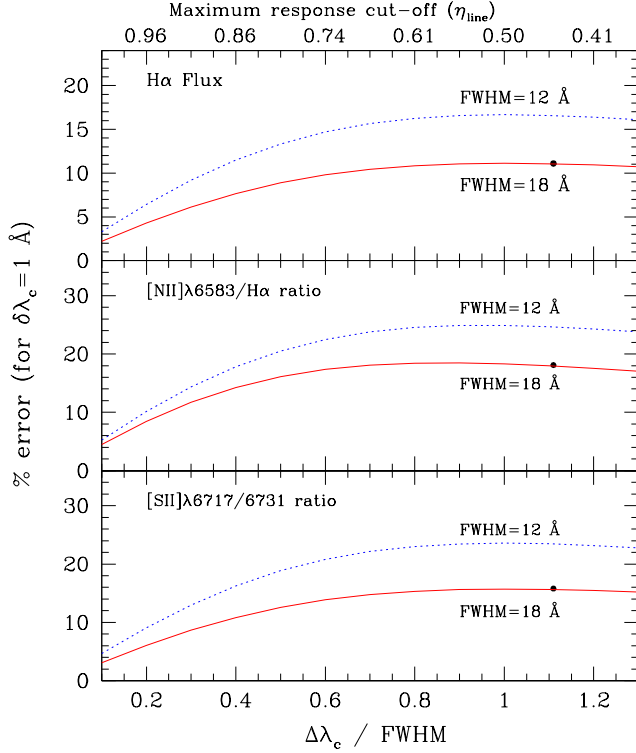


FIG. 3.— Errors in flux and flux ratios due to an uncertainty of $\delta\lambda_c = 1 \text{ \AA}$ in setting the central wavelength of TF, as a function of user-selected TF parameters $\Delta\lambda_c$ and FWHM. The errors are expressed as percentage values of the plotted quantity. (top) Errors on the $H\alpha$ flux, (middle) errors on the $[\text{N II}]\lambda 6583/H\alpha$ ratio, and (bottom) errors on the $[\text{S II}]\lambda 6717/6731$ ratio. The scale on the top gives the maximum value of response cut-off (η_{line}) that the data permit for given values of $\Delta\lambda_c$ and FWHM, without having data gaps in the reconstructed image (see §4.1 for details). Errors expected in our dataset of M101 for an assumed error of $\delta\lambda_c = 1 \text{ \AA}$ are marked by solid circles.

the observations of an extended emission line source with a scanning TF, making use of Eqs. 1 and 2. The simulated dataset also allowed us to quantify the accuracy of reconstruction to various instrumental parameters that have non-zero uncertainties. Two scans were simulated: (1) TF with a FWHM=18 \AA , $\lambda_c = 6528 + (i - 1) \times 20 \text{ \AA}$, where i varied from 1 to 9, (2) TF with a FWHM=12 \AA , $\lambda_c = 6528 + (i - 1) \times 10 \text{ \AA}$, where i varied from 1 to 18. The reddest wavelength in both cases is 6688 \AA . The FWHM in the two settings are among the extreme values permitted with the red etalon, with the former one simulating the dataset we have for M101. The intensity of the extended source is set constant over the FoV of OSIRIS with $I(H\alpha)=1$. The $[\text{N II}]\lambda 6583$ line is fixed at 10% of that of $H\alpha$, which is among the range of values observed in H II regions (Denicoló et al. 2002). The $[\text{N II}]\lambda 6548$ line intensity is fixed at one third of that of the $[\text{N II}]\lambda 6583$ line. We also added continuum sources at some fixed positions on the image, in order to test the accuracy of the continuum subtraction. The intensities of the continuum sources are adjusted such that the $H\alpha$ emission equivalent widths at the positions of the continuum sources are 10 for some sources and 100 for others. Gaussian noise of two different values is added

to the images, resulting in two sets of simulations: the high and low Signal-to-Noise Ratio (SNR) images correspond to SNRs of 100 and 3 for the $[\text{N II}]\lambda 6583$ line image, respectively. A line-free continuum image is also generated in the simulated set. The lines were redshifted by 214 km s^{-1} , corresponding to the recession velocity of M101.

5.3. Parameters that limit the reconstruction accuracy

Reconstruction with ideal datasets (Run 0): The equations described in §3 should allow us to recover the fluxes of the $H\alpha$ and $[\text{N II}]\lambda 6583$ lines, in the absence of uncertainties in various parameters that control the TF imaging. We simulated this case by using high SNR data and subtracting the simulated line-free continuum. The errors in recovering the $H\alpha$ flux and the flux ratio $[\text{N II}]\lambda 6583/H\alpha$ are as small as 0.03% and 0.2% respectively. This test establishes that the equations developed in §3 are correctly implemented in the script.

However, there are many sources of error in real observational datasets, especially when trying to maximize the available observing time. We investigate the accuracy in the recovered flux due to the following 3 sources of error: (1) the continuum images are not completely free of emission lines, (2) the sky images are obtained by in-frame object-free pixels, not from an off-source sky image, (3) different images within a scan have non-zero ditherings. We discuss each of these cases in detail below.

Line contamination in continuum images (Run 1): Due to the long tail of the TF response, there is non-zero line contribution in all TF images, including those centered bluer than the bluest line in a scan (e.g., $\lambda_c = 6528$ is only ~ 1 FWHM blueward of the $[\text{N II}]\lambda 6548$ line, and < 2 FWHMs of the bright $H\alpha$ line). In order to obtain line-free continuum fluxes from the sequence of images we have, we followed the iterative procedure described in §4.3. We obtained a continuum image from the sequence of simulated images, and compared it to the simulated pure continuum image. The difference between the two images is found to be as small as 0.1% after 3 iterations. Hence, errors on the fluxes in our reconstructed images of M101 are not dominated by the limitations of obtaining line-free continuum images.

Non-uniform sky (Run 2): Errors in sky value subtraction and flat-field corrections introduce residuals in the sky value locally. We parametrized this error in terms of the rms noise value (σ) of this image. The residual sky value in different parts of the image is allowed to vary between -1σ and $+1\sigma$, for the simulated set of images. The $[\text{N II}]\lambda 6583/H\alpha$ ratios are affected by 5% in pixels where $[\text{N II}]\lambda 6583$ is detected with a SNR of 3. Thus, for pixels with $\text{SNR} > 3$ for the line of $[\text{N II}]\lambda 6583$, sky subtraction is not a serious problem in our images of M101.

Consequences of Image-dithering (Run 3): It is a normal practice to dither images between any two repeat observations in order to avoid detector blemishes spoiling any interesting feature. These dithered images are registered to a common coordinate system before combining them. In a TF observation, the optical centers in the dithered images correspond to different astrometric coordinates and hence the corresponding pixels in the registered images do not have the same wavelength (see Eq. 1). Thus, in the combined image, a given pixel has contributions from marginally different wavelengths. We

parametrized this effect as an error in the optical center δr_c . We studied the reconstruction accuracy for various values of δr_c between $1''$ and $5''$. A dithering of $1''$ between different images of a scan can produce errors of the order of $\sim 5\%$ in the recovered $H\alpha$ flux for the $FWHM=18 \text{ \AA}$ filters. The recovered $[N II]\lambda 6583/H\alpha$ ratio lies between 0.05–0.15 (50% error over the simulated value of 0.1) for this case. Combining images that are dithered by more than $1''$ would introduce more than 20% error on the recovered $H\alpha$ flux, making it unusable for most applications. In the case of our observations of M101, the dithering within a scan was less than $0.25''$, and hence the error in the recovered $H\alpha$ flux due to astrometric registration of all images of a scan (say P1) is less than a few percent.

5.4. Recommendations for observing extended sources

After studying the effect of various parameters on the fluxes in the reconstructed images, we find that the maximum error on our dataset for M101 arises due to the present uncertainty of $\sim 1 \text{ \AA}$ in setting the central wavelength of a TF observation. This uncertainty affects more the images taken with narrower TF observations, with the accuracy of $H\alpha$ fluxes being $\sim 10\%$ and of $[N II]\lambda 6583/H\alpha$ ratios of $\sim 18\%$ for the TF images with $FWHM = 18 \text{ \AA}$, as can be inferred from Fig. 3. Corresponding errors with $FWHM = 12 \text{ \AA}$ are 16% and 25%, respectively. Errors may be reduced by carrying out the scan with a finer sampling. With $FWHM = 12 \text{ \AA}$ a sampling of around 5 \AA would be required to reduce the error levels to $\sim 10\%$, that can be achieved with 15 \AA sampling with $FWHM = 18 \text{ \AA}$. Thus a factor of 3 more exposure time would be required to map a given emission line over the entire FoV of OSIRIS with the narrower TF. However, for low SNR pixels or regions for which sky and/or continuum subtraction errors contribute more than the plotted errors ($SNR \lesssim 10$), the errors are expected to increase proportionally with the FWHM, and hence observations with $FWHM = 12 \text{ \AA}$ would have an advantage by a factor of 1.5 over those with $FWHM = 18 \text{ \AA}$. Thus, if the interest is in detecting diffuse faint emissions, a $FWHM = 12 \text{ \AA}$ is preferable.

Lara-López et al. (2010) carried out simulations to determine the best combination of FWHM and sampling ($\Delta\lambda_c$) for optimal emission line flux determinations of emission-line galaxies of redshifts between 0.2 and 0.4 with GTC/OSIRIS. They found that a FWHM of 12 \AA and a sampling of 5 \AA are the optimal combination that allows deblending $H\alpha$ from the $[N II]\lambda 6583$ line with a flux error lower than 20%. It is relevant to note that in their simulations, the fluxes were not corrected for the response curve of the TF, and the quoted flux errors are due to the unavailability of the redshifts of the detected galaxies. Hence, it is natural to expect lesser errors for the narrower filters.

The next source of error comes from image dithering. For an image dithering of $1''$, the errors could be as large as 5% for $H\alpha$ and 50% for $[N II]\lambda 6583/H\alpha$. For larger values of dithering, errors on $[N II]\lambda 6583/H\alpha$ are unreasonably high. It is advisable to have the same telescope position (dithering $< 1''$) for all the images constituting a given TF scan. If more than one scan is available for a field with dithering of more than $1''$ between the scans,

it is advisable to reconstruct an emission-line image from each scan, and then register and combine them. We recommend that a TF scan intended to obtain a monochromatic image in an emission line should have one image observed at least one $FWHM$ blueward of the bluest line in the TF sequence, to facilitate accurate continuum subtraction.

6. FLUX CALIBRATION OF MONOCHROMATIC IMAGES

We have explored a new procedure to flux calibrate the TF images using the in-frame field stars. The procedure, in principle, can be applied to any optical narrow-band image of a field that contains stars with photometry in the optical broad-bands. In particular, we used the SDSS photometry in *griz* bands of stars in the field of M101, and the recently released SDSS Stellar Spectral database of stars covering a wide range of spectral types (Abazajian et al. 2009). These spectra are of median resolution in the $3500\text{--}9000 \text{ \AA}$ wavelength range. In order to have a good spectral library we selected, from the original Stellar Spectral database, only those stars with $g = 14\text{--}18$ mag having no gaps, jumps or emission lines in their spectra.

The general procedure involves obtaining a stellar spectrum that fits the *griz* magnitudes of the stars in the field of the TF image. Basically, we are using the stellar spectrum to interpolate the broad-band fluxes at the wavelength of the TF. The spectra are integrated in the *griz*-bands to get their synthetic magnitudes which are then fitted to the *griz* magnitudes of a star in the field of interest; both Spectral Energy Distributions (SEDs) are normalized at the *r*-band.

The best-fit spectrum is chosen by minimizing the χ^2 obtained in the 4 bands. The spectrum of the best-fit SDSS star is then de-normalized by multiplying it by the *r*-band flux of the field star. The resulting spectrum is convolved with the response function of the OSIRIS TFs (Eq. 2) to obtain a smoothed spectrum of the field star. The flux at λ_r , where r is the radial distance of the star in the OSIRIS field, is multiplied by the effective bandwidth of the TF, to estimate the flux intercepted by the TF.

We then carried out aperture photometry of the selected SDSS stars on all the TF images. This photometry is used to obtain observed count rate of each star in each TF image. The estimated flux is divided by the observed count rate of the star in that TF to obtain the calibration coefficient κ . The procedure is repeated for all the good SDSS stars in the observed field to obtain a set of κ values. We note that the observed count rate is initially corrected for the effects of extinction and the efficiency of the order sorter filter, and hence the κ obtained from different stars in different TFs can be directly compared with each other.

6.1. Relative errors in the Calibration coefficients

The availability of thousands of stellar spectra covering the entire range of spectral types to fit the photometric data of field stars ensures that there is at least one spectrum that truly represents the spectrum of the field star. Generally, there are 10–15 spectra whose *griz*-band χ^2 is within 10% of the best-fit spectrum. We obtained a mean and rms of these spectra at every sampled wavelength. The rms error was found to be less than 1% for

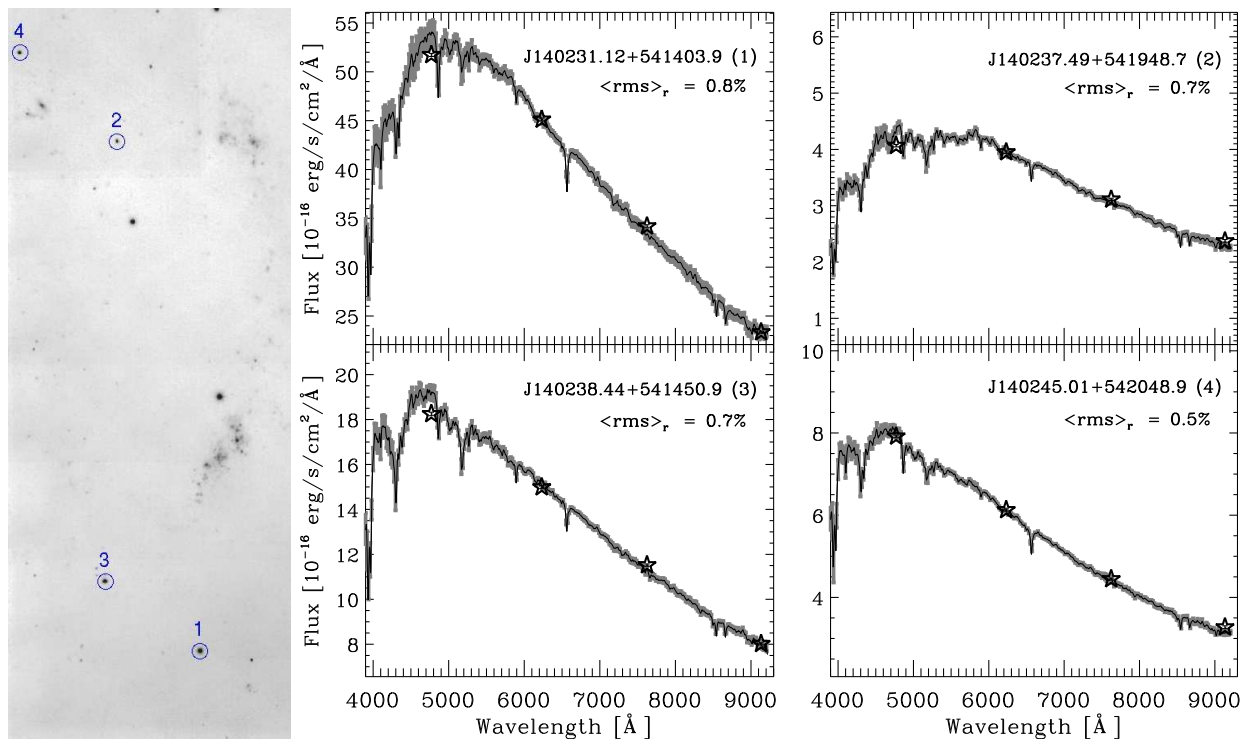


FIG. 4.— An illustration of the calibration procedure adopted, where we fit the SDSS *griz* photometry of in-frame field stars with the spectra of stars in the SDSS spectral catalog. (left) A section of the OSIRIS continuum image of M101. Four stars with SDSS photometry are identified. (right) SEDs in *griz* bands of the 4 identified stars (asterisk), superposed on the average of 12 best fitting spectra from SDSS spectral catalog (line). The rms deviation from the mean of 12 best-fit spectra at each wavelength is shown by the gray band around the mean spectrum. The 12 spectra differ by less than 1% ($\langle rms \rangle_r$ denotes the average rms value within the *r*-band), which makes this method very attractive for the calibration of OSIRIS TF data.

wavelengths between the *g* and *z* bands. Thus the relative flux calibration for different TF settings is better than 1%. The absolute flux error depends on the error in the SDSS *r*-band magnitude of the field stars. An illustration of the method followed is shown in Fig. 4.

In Fig. 5, we show the variation of the calibration coefficient along an $H\alpha$ TF scan containing 9 images. In this figure, two kinds of systematic variations are seen: (1) the variation of the coefficient from one TF observation to the next, and (2) the variation of the coefficient between the two CCDs.

Variation of calibration coefficient during a TF scan: given that the airmass variation from one observation to the next is taken into account in obtaining the κ , this variation was not expected for a photometric night. The rms dispersion for the 4 stars that are used to calculate κ is around 3%, which is much smaller than the overall variation (9% over the mean value). The trend of the variation is identical for the two scans.

Variation of calibration coefficient between the two CCDs: OSIRIS uses two CCDs, along with 2 separate electronics to cover the total field of view. The differences in the background levels between the two CCDs are easily noticeable. From our analysis, we find that there is a $6 \pm 3\%$ difference between the efficiencies of the two CCDs for the $H\alpha$ scan. The most likely rea-

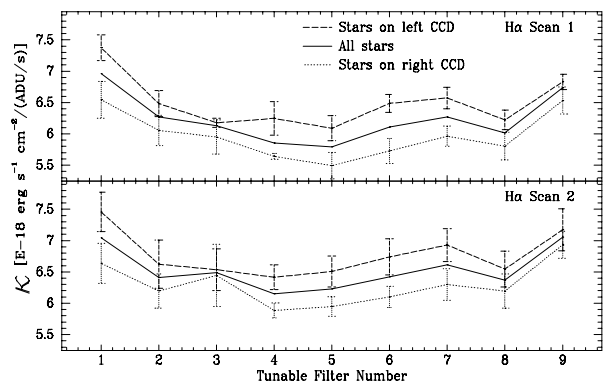


FIG. 5.— Variation of the calibration coefficient κ for 9 images of the two $H\alpha$ TF scans of M101. We used 8 stars, 4 on each CCD covering the complete field of view. The coefficients for the right (dashed line) and left (dotted line) CCDs are separately shown. The solid line shows the variation without distinguishing on which CCD stars are located. In the top panel, we show the coefficients for scan 1 (P1) and in the bottom, for scan 2 (P2).

son for this difference is the value of the gain parameter,

TABLE 2
DERIVED VALUES OF CALIBRATION COEFFICIENTS

TF Scan	κ	Units
H α + [N II]-P1	$6.54 \pm 0.27 \cdot 10^{-18}$	$\text{erg s}^{-1} \text{cm}^{-2}/(\text{ADU/s})$
H α + [N II]-P2	$6.63 \pm 0.28 \cdot 10^{-18}$	$\text{erg s}^{-1} \text{cm}^{-2}/(\text{ADU/s})$
S II-P1	$7.06 \pm 0.14 \cdot 10^{-18}$	$\text{erg s}^{-1} \text{cm}^{-2}/(\text{ADU/s})$
S II-P2	$7.06 \pm 0.21 \cdot 10^{-18}$	$\text{erg s}^{-1} \text{cm}^{-2}/(\text{ADU/s})$
S II-P3	$7.27 \pm 0.23 \cdot 10^{-18}$	$\text{erg s}^{-1} \text{cm}^{-2}/(\text{ADU/s})$

which is 0.95 electrons/ADU for the right CCD and 0.91 electrons/ADU for the left CCD (private communication from GTC technical staff) during the H α scan.

When these systematic variations in κ are taken into account, the calibration coefficients obtained using different stars in different CCDs and in different TF images, agree to within 3% of each other. The mean calibration coefficients obtained from the stars on the right CCD of the first image of the H α and [S II] scans are given in Table 2. The difference in the calibration coefficients for the two H α scans is of the order of 1%, whereas for the [S II] scans this difference is around 3%. The mean difference in the calibration coefficients for the H α and [S II] scans is $\sim 7\%$. The κ factors in the reconstruction equations take into account both these systematic variations, thus allowing us to combine the monochromatic images from different images of a scan.

7. COMPARISON OF RECONSTRUCTED IMAGES

In Fig. 6, we show the reconstructed H α emission-line image of the south-west part of M101. The H α line being a good tracer of ionized gas, this image shows the location of H II complexes and ionized filaments. It can be seen from the image that we are able to detect H II regions in the entire field of view. The 5σ surface brightness limit in this image is $8 \times 10^{-17} \text{ erg cm}^{-2} \text{ s}^{-1} \text{ arcsec}^{-2}$. All the regions seen in the image are recovered in the two independent scans. In the following paragraphs, we compare the fluxes of recovered emission lines of H II regions in these two independent scans. Our H α fluxes are also compared with the H α fluxes obtained using traditional narrow-band imaging technique.

We performed photometry of 23 H II regions using an aperture radius of $4''$ on our reconstructed H α , [N II] $\lambda 6583$, [S II] images and also on an H α + [N II] image that was obtained in the traditional way using narrow-band filters (downloaded from NED: Telescope: KPNO Schmidt; Observers: B. Greenawalt, and R. Walterbos). The selected regions are among the brightest regions in the FoV.

With a sampling of $\Delta\lambda_c = 20 \text{ \AA}$ for our dataset, η_{line} should be at least 0.45 in order to obtain an image without data gaps. However, we found systematically larger dispersion in fluxes for regions with response values less than 0.5. Therefore we carried out the reconstruction with $\eta_{\text{line}} = 0.5$. As a result, eight regions have data in only one of the dithered scans. In Fig. 7a, we show a comparison of the fluxes of the 15 H II regions whose fluxes could be measured on the reconstructed images from both the scans. The mean ratio of the H α fluxes is unity over 2 orders of magnitude in flux, confirming the accuracy of the method we adopted for the flux calibration. The rms dispersion of the H α fluxes of the same

region obtained on images for the two scans is 16%. This value is within the flux errors expected for the 1–2 \AA error in λ_c .

In order to check whether the reconstruction process rightly reproduces relative fluxes of different regions over the entire FoV, we plot the ratio of the H α + [N II] $\lambda 6583$ fluxes measured from our reconstructed images (P1 and P2), and that from traditional narrow-band filters in Fig. 7b. Our fluxes are given as the average when data are available from both scans. As the intention here is a comparison of relative fluxes, we set the mean value of the flux ratio to unity. There is $\sim 11\%$ scatter on this mean value, which is marginally better than that between P1 and P2, as expected due to the use of averaged fluxes. There is a marginal trend for the mean ratio to be $\sim 5\%$ different between the bright and faint regions, which is nevertheless smaller than the scatter. We did not find any trend of these two ratios against the distance of the region from the optical center.

Three sources of error are included in calculating the sizes of the error bars plotted in Fig. 7. They are (1) photon noise of the object, (2) the error in the subtraction of the sky value and (3) the error in the recovered flux due to an error in λ_c . The last of these errors, which is discussed in detail in §5, dominates for the 23 regions for which we performed photometry, contributing around 10% for the majority of the regions.

As a second test of the reliability of the flux ratios obtained using the TF images, we compare the flux ratios of emission lines relevant for diagnostic diagrams with those values obtained using spectra from the literature for the same regions. Seventeen H II regions in M101 were observed spectroscopically by SDSS (Sholudchenko et al. 2007). Six of these lie within the usable FoV of our images (radial distance from the optical center $\lesssim 3.75'$). Flux ratio of nebular diagnostic lines from our reconstructed images are compared with those obtained from the SDSS spectra in Fig. 8. Our fluxes were obtained over apertures of $4''$ radius at the coordinates associated with the SDSS spectra. The adopted apertures, though almost 3 times bigger than the fiber sizes of SDSS spectra ($3''$ diameter), are the minimum area over which reliable fluxes can be measured in our images. Given that the spectroscopic ratios of giant H II regions are not expected to vary much with aperture size, our relatively bigger apertures are not expected to introduce additional errors. The difference in the flux ratios between ours and SDSS values are plotted both against flux ratios (in the left panel) and H α fluxes (in the right panel). The plotted error bars take into account all the errors discussed in the paragraph above. The errors in the spectroscopic ratios are expected to be almost negligible, and hence we did not include these errors in our analysis. The majority of the points lie close to the horizontal line within the plotted errors, indicating that the ratios of lines relevant for diagnostic purposes can be obtained using TF imaging. There are a few ratios that deviate from the spectroscopic ratios by more than the estimated errors. The most important of them is the right-most point in panel (a). Apart from being the faintest in H α , the spectroscopic [N II] $\lambda 6583$ /H α value for this region is 0.4, a value that is too high as compared to the assumed value of 0.1 in Eqn 10. This is the most likely reason for the large deviation of this region. Kinematics of individual regions

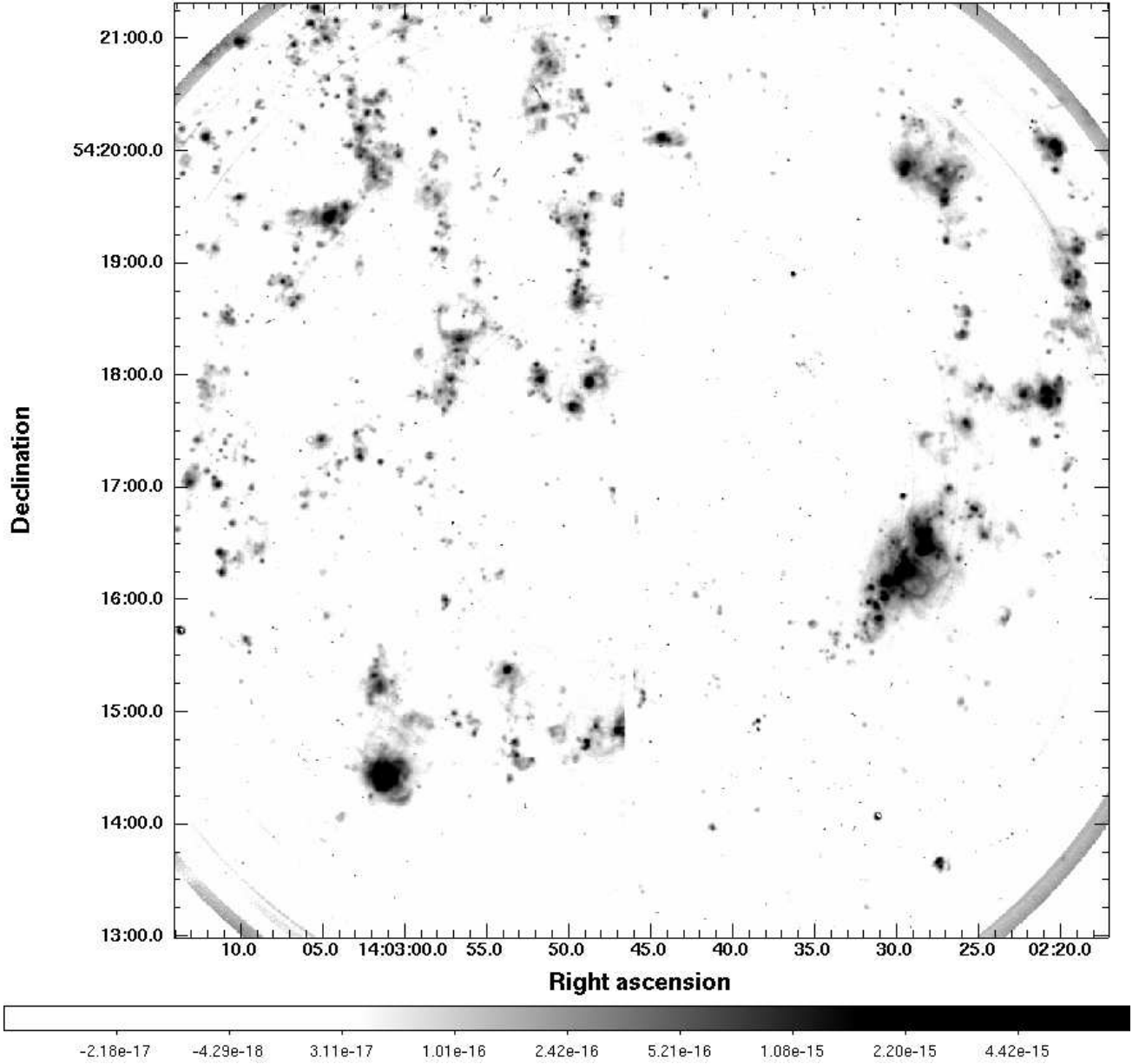


FIG. 6.— Reconstructed $H\alpha$ image of the south-west part of M101. Several $H\text{ II}$ regions, including the massive $H\text{ II}$ complex NGC 5447 ($\alpha = 14 : 02 : 30, \delta = 54 : 16 : 15$), as well as several filamentary structures can be seen in this image. The brightness of the $H\alpha$ structures is shown by the gray bar at the bottom of the image in units of $\text{ergs}^{-1} \text{cm}^{-2} \text{arcsec}^{-2}$, spanning a range from -3σ to 512σ in logarithmic scale.

with radial velocities $> 25 \text{ km s}^{-1}$ (i.e. 0.5 \AA around the $H\alpha$ wavelength) can also be responsible for the observed deviations of some of the points. The errors in the measured radial velocities of the regions from SDSS spectra do not permit us to carry out a more elaborate analysis of the deviations of individual regions.

In summary, the ratios recovered from the TF images for individual regions have larger errors than the corresponding spectroscopic ratios. Nevertheless, the capability of TF images to derive such ratios for large number of regions, makes TF imaging a scientifically attractive option, as we illustrate below using the flux ratio of 23 $H\text{ II}$ regions in M101.

In Fig. 9, we plot the $[\text{N II}]\lambda 6583/H\alpha$, $[\text{S II}]\lambda 6716 + \lambda 6731/H\alpha$, and the $[\text{S II}]\lambda 6716/\lambda 6731$ ratio of $H\text{ II}$ regions against their $H\alpha$ fluxes in panels (a), (b) and (c), respectively. In each of these panels, we indicate the observed/theoretical ranges of these ratios in $H\text{ II}$ regions, which cover ~ 10 times the errors on the ratios. This relatively large dynamic range, combined with the intrinsic multi-object capability of TF imaging, makes it competitive with traditional spectroscopic observations.

The $[\text{N II}]$ and $[\text{S II}]$ lines originate in low ionization zones in $H\text{ II}$ regions. Their ratio to the $H\alpha$ flux depends not only on the ionization parameter, but also on the abundance of these ions. The utility of these ratios for

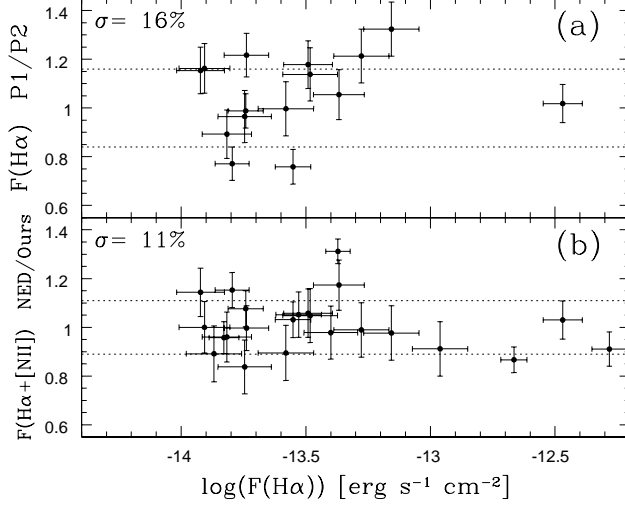


FIG. 7.— Relative errors on the $H\alpha$ fluxes of 23 H II regions in M101. (a) Ratio of the $H\alpha$ fluxes measured on the reconstructed image for the dithered position P1 to those for position P2; (b) ratio of the H II region fluxes measured on an $H\alpha$ + $[N II]$ image taken from NED to those on our images, both plotted against our $H\alpha$ fluxes. The dotted horizontal lines denote 1σ scatter over the mean ratio.

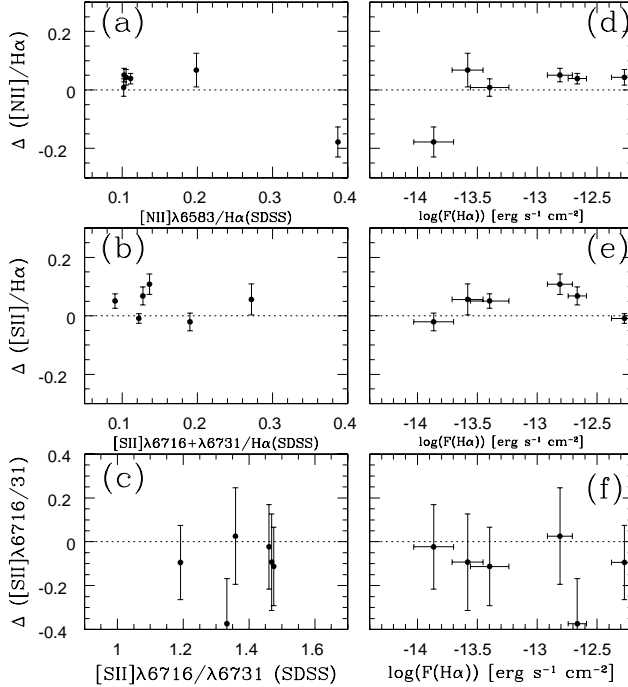


FIG. 8.— Comparison of important diagnostic ratios from our reconstructed images with those obtained using SDSS spectra for 6 regions in common. In the left panels the difference between the ratios (e.g. $\Delta([N II]/H\alpha) = ([N II]\lambda 6583/H\alpha)_{\text{ours}} - ([N II]\lambda 6583/H\alpha)_{\text{SDSS}}$) is plotted against the SDSS ratios, whereas in the right panels, the difference between the ratios is plotted against our $H\alpha$ fluxes. In general, the diagnostic ratios are reproduced within the ranges allowed by the estimated errors. See text for more details.

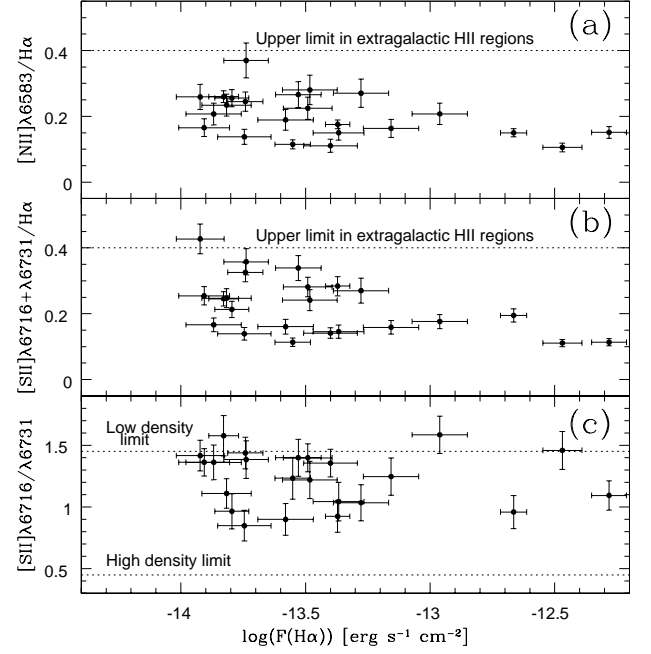


FIG. 9.— Flux ratios of nebular diagnostic lines plotted against the $H\alpha$ fluxes for the 23 H II regions of Fig. 7. In panels (a) and (b), we show $[N II]\lambda 6583/H\alpha$ and $[S II]\lambda 6716 + \lambda 6731/H\alpha$, whereas in panel (c) we show the density-sensitive ratio $[S II]\lambda 6716/\lambda 6731$. The upper limits observed in extragalactic H II regions from Denicoló et al. (2002) are indicated by the horizontal dotted lines in the top two panels, whereas the theoretically valid range for the $[S II]$ line ratios from Osterbrock & Ferland (2006) is shown in panel (c). All the regions have observed ratios in the range expected for H II regions, illustrating the capability of TF imaging for obtaining these diagnostic ratios.

diagnostic purposes has been discussed in Baldwin et al. (1981). In Fig. 10, we show the values for these ratios expected for a range of ionization parameters (R) and metallicities (Z), using the models of Dopita et al. (2006). The observed values of these ratios in our selected 23 regions lie within the range of model values. The regions having high values of $[N II]/H\alpha$ have most likely high nitrogen abundances, as was found by Denicoló et al. (2002) for H II regions in a sample of nearby galaxies. Thus, OSIRIS TF imaging is very promising for the study of nebular line ratio diagnostics of nearby large galaxies.

8. SUMMARY

In this work, we have explored the capability of tunable filter imaging with the OSIRIS instrument at the 10.4-m GTC, using real data. The changing wavelength across the field and the non-flat functional form of the response curves makes it essential to have a sophisticated analysis package to completely take advantage of the relatively large field of view of the instrument. With the set-up that we have used to observe M101, we were able to obtain monochromatic images in the emission lines of $H\alpha$, $[N II]\lambda 6583$ and the $[S II]$ doublet. We demonstrate that line fluxes and their ratios for prominent H II regions can be obtained to better than $\sim 15\%$, which is basically limited by the current 1 \AA uncertainty in setting the central wavelength of the TF. Though these errors are much larger than the spectroscopic ones, the multi-object ca-

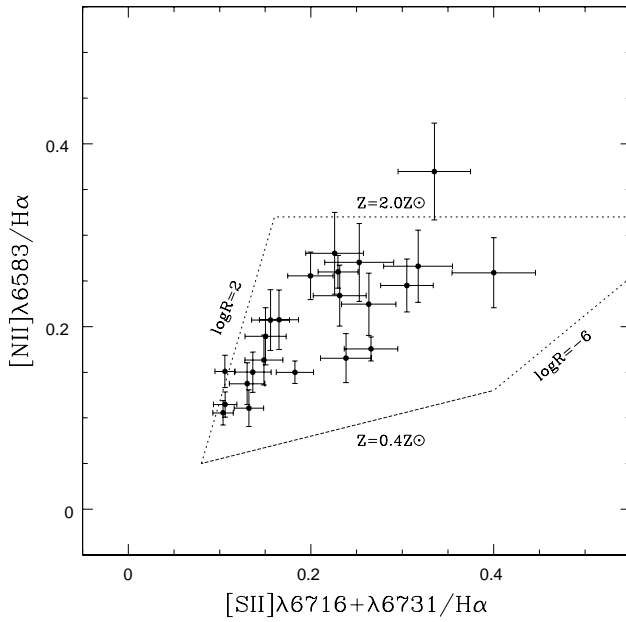


FIG. 10.— Nebular diagnostic diagram involving $[N II]\lambda 6583/H\alpha$ and $[S II]\lambda 6716/\lambda 6731$ for H II regions in M101. All the observed points lie within loci of models of Dopita et al. (2006) defined by metallicities between $0.4Z_{\odot}$ and $2Z_{\odot}$, and the logarithmic ionization parameter $\log R$ between 2 (low pressure regions) and -6 (high pressure regions).

pability of TF imaging, combined with the relatively high sensitivity of the flux ratios to variations in density, excitation and metallicity, makes TF imaging an attractive option for investigating the point-to-point variation of these physical quantities in galaxies. We also demonstrate that the emission-line maps can be flux-calibrated to better than 3% accuracy, using the *griz* SDSS magnitudes of in-frame stars, and the spectral database of SDSS, without the need to invest extra telescope time to perform the photometry of spectrophotometric stars.

It is a pleasure to thank an anonymous referee, whose thoughtful comments helped us to improve the original manuscript. We would also like to thank the GTC/OSIRIS staff members, especially Antonio Cabrera, for the support provided for this project. This work is partly supported by CONACyT (Mexico) research grants CB-2010-01-155142-G3 (PI: YDM), CB-2011-01-167281-F3 (PI: DRG), CB-2005-01-49847 and CB-2010-01-155046 (PI: RJT), and CB-2008-103365 (PI: ET). This work has been also partly funded by the Spanish MICINN, Estallidos (AYA2010-21887, AYA2007-67965) and Consolider-Ingenio (CSD00070-2006) grants.

REFERENCES

- Abazajian, K. N., Adelman-McCarthy, J. K., Agüeros, M. A., et al. 2009, *ApJS*, 182, 543
- Baldwin, A., Phillips, M. M., & Terlevich, R. 1981, *PASP*, 93, 817
- Beckers, J. M. 1998, *A&AS*, 129, 191
- Beers, T. C., Lee, Y., Sivarani, T., et al. 2006, *Mem. Soc. Astron. Italiana*, 77, 1171
- Born, M., & Wolf, E. 1980, *Principles of Optics Electromagnetic Theory of Propagation, Interference and Diffraction of Light* by Max Born, Emil Wolf Oxford, GB: Pergamon Press, 1980,
- Cepa, J., Aguiar, M., Castañeda, H. O., et al. 2005, *Revista Mexicana de Astronomía y Astrofísica Conference Series*, 24, 1
- Cepa, J. 2010, *Highlights of Spanish Astrophysics V*, 15
- Denicoló, G., Terlevich, R., & Terlevich, E. 2002, *MNRAS*, 330, 69
- di Césare, M. A., Hammersley, P. L., & Rodríguez-Espinosa, J. M. 2007, *The Future of Photometric, Spectrophotometric and Polarimetric Standardization*, 364, 289
- Dopita, M. A., Fischera, J., Sutherland, R. S., et al. 2006, *ApJS*, 167, 177
- Jones, D. H., Shopbell, P. L., & Bland-Hawthorn, J. 2002, *MNRAS*, 329, 759
- Lara-López, M. A., Cepa, J., Castañeda, H., et al. 2010, *PASP*, 122, 1495
- Méndez-Abreu, J., Sánchez Almeida, J., Muñoz-Tuñón, C., et al. 2011, *PASP*, 123, 1107
- Osterbrock, D. E., & Ferland, G. J. 2006, *Astrophysics of gaseous nebulae and active galactic nuclei*, 2nd. ed. by D.E. Osterbrock and G.J. Ferland. Sausalito, CA: University Science Books, 2006,
- Rangwala, N., Williams, T. B., Pietraszewski, C., & Joseph, C. L. 2008, *AJ*, 135, 1825
- Rosales-Ortega, F. F., Kennicutt, R. C., Sánchez, S. F., et al. 2010, *MNRAS*, 405, 735
- Sholudchenko, Y. S., Izotova, I. Y., & Pilyugin, L. S. 2007, *Kinematics and Physics of Celestial Bodies*, 23, 163
- Veilleux, S., Weiner, B. J., Rupke, D. S. N., et al. 2010, *AJ*, 139, 145